UCLA

UCLA Electronic Theses and Dissertations

Title

Optimizing a Radio-Frequency Coil for Pituitary Gland Imaging at 3 Tesla Magnetic Resonance Imaging

Permalink

Author

Ruan, Huaijin

Publication Date

2022

Peer reviewed|Thesis/dissertation

UNIVERSITY OF CALIFORNIA

Los Angeles

Optimizing a Radio-Frequency Coil

for Pituitary Gland Imaging at 3 Tesla Magnetic Resonance Imaging

A thesis submitted in partial satisfaction

of the requirements for the degree Master of Science

in Electrical and Computer Engineering

by

Huaijin Ruan

2022

ABSTRACT OF THE THESIS

Optimizing a Radio-Frequency Coil

for Pituitary Gland Imaging at 3 Tesla Magnetic Resonance Imaging

by

Huaijin Ruan

Master of Science in Electrical and Computer Engineering

University of California, Los Angeles, 2022

Professor Robert N. Candler, Chair

Magnetic resonance imaging (MRI) can serve as an efficient tool to examine the internal

structure of the human body, especially for soft tissues. The pituitary gland – which regulates

hormones in the body – is one example of soft tissue that can be investigated by MRI [1].

One area of particular interest in the study of the pituitary gland is the search for miniature

tumors, also called microadenomas. Microadenomas in the pituitary gland are important

because they can cause Cushing's disease, which can cause death if untreated [2]. However,

although 60-80% of the pituitary adenomas are microadenomas [3], current 3 T MRI

techniques cannot detect up to 50% of the microadenomas [4]. The present work aims to

increase detection accuracy by placing miniaturized MRI coils inside the sphenoid sinus (a hollow space or cavity near the pituitary gland), as close as possible to the region of interest (ROI), namely the pituitary gland [5]. By placing MRI surface coils close to the target region, the SNR can be increased, which allows for improved detection accuracy of microadenomas that are too small for current scanning techniques. Previous studies using single-loop surface coils achieved high-SNR images, but in some cases, coils need to be rotated so that they can fit into the cavity near the pituitary gland. In the case of large rotation angles, single-loop surface coils are limited by the intrinsic "dead spot", especially when rotated 90 degrees [4]. In contrast, figure 8-shaped surface coils are less effected by the signal loss due to coil plane rotations [6]. In this study, we developed a custom-designed surface coil specifically for pituitary gland imaging. Parameters of the coil are optimized based on simulations, including the distance between the two semicircle-shaped components and the coil radius. A linear relationship between the optimal coil radius and target depth is established. The compensation between rotation angle of the coil plane and the horizontal shift of the target is also studied, proving that rotations have a reduced detrimental effect on coil performance as compared to single-loop coils, especially when the target is placed near the coil boundary.

The thesis of Huaijin Ruan is approved.

Sam Emaminejad

Clarice Demarchi Aiello

Robert N. Candler, Committee Chair

University of California, Los Angeles

2022

List of Contents

List of Figures

List of Tables

1. Introduction

Tomography has been proved to be essential in imaging. It provides ways to generate three-dimensional images of the internal structures of a solid body, while avoiding making physical damage to the study subject. Tomographic imaging techniques for medical and non-medical uses have been thoroughly explored, including X-ray Computer Tomography (CT), Magnetic Resonance Imaging (MRI), Positron Emission Tomography (PET), Single Photon Emission Computed Tomography (SPECT), and many more [7]. Among these imaging modalities, here we focus on MRI.

Physically, MRI is an application of Nuclear Magnetic Resonance (NMR) phenomena [8]. By applying spatial information encoding principles, the image extraction based on NMR signals becomes possible. Compared to other imaging methods, MRI has several advantages: (1) it can generate two-dimensional sectional images at arbitrary orientations; (2) it avoids injecting radioactive isotopes into the object for signal generation, and thus reduces potential harmful effects; (3) the resulting spatial resolution is not limited by the working frequency range [7]. Due to these properties, the technique of MRI has been employed for disease diagnosis that requires examining the subtle inner structures of patients' body [9], [10].

To obtain clear images in a fast manner, there was once a shift in interest from 1.5 T to 3 T in clinical practice several decades ago [11]. Nowadays, the clinical use of 3 T MRI systems for brain, musculoskeletal, body, cardiovascular, and other applications has been widely adopted around the world [12]. Similarly, there has been steady progress in NMR receiving systems, which was first discussed by Hoult back in 1978 [13].

Researchers soon noticed that fitting small coils to a ROI would allow a more localized and

thus higher signal-to-noise ratio (SNR) [5]. In 1980, Ackerman et al. first discovered that a significant SNR gain can be achieved when placing a small surface-coil on the surface of the sample and thus making the coil close to the ROI [14]. Although many radiofrequency (RF) coil designs have been proposed in recent years, we may still classify them into three major categories based on the specific uses, namely: volume coils, surface coils, and array coils.

1.1. Research Objectives

In this study, we will mainly focus on the optimization of a surface coil for imaging the pituitary gland in 3 T MRI. The pituitary gland is a pea-sized endocrine gland located at the base of the brain, producing essential hormones to regulate the daily behaviors of the body [15]. Pituitary adenomas can be distinguished by both excess proliferation of one of the differentiated cell types of the anterior pituitary and dysregulated hormone hypersecretion [15]. Cushing's disease (CD) is caused by an adrenocorticotropin hormone (ACTH)-producing pituitary tumor, but due to variations in the size of pituitary tumors, up to 50% of the microadenomas in this disease cannot be detected in the standard setup for 3 T MRI [4]. To deal with the problem, a miniature flexible coil for high-SNR MRI of the pituitary gland was proposed [4]. However, although SNR improvement is achieved, the traditional single-loop miniature flexible coil mentioned in [4] possesses the limitation of angle-dependence, which would essentially lead to a dead spot in the image when the coil is rotated 90 degrees due to clinical needs.
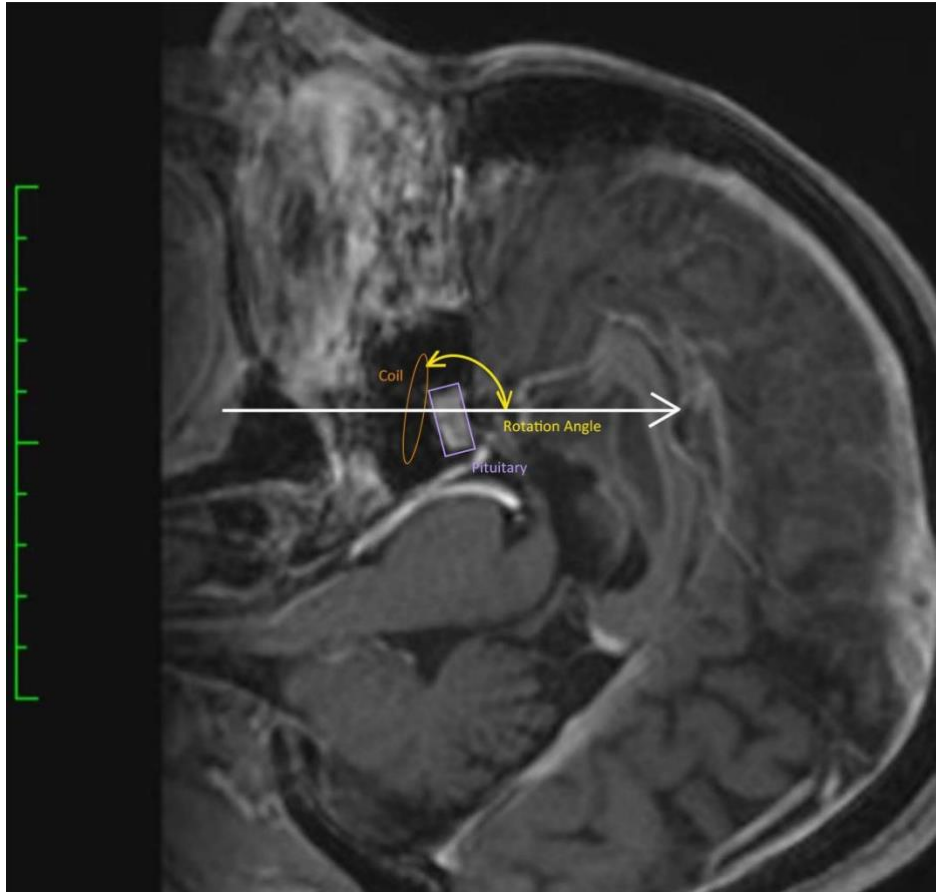
Figure 1.1 Rotation angle required for clinical needs.

To address this limitation, in this work, we optimize a RF surface coil that is specifically designed to achieve high-SNR at various coil rotation angles. The proposed optimization is simulation-based, and experimental validation will be the future work that follows the completion of this thesis.

The major goal of this study is to find an optimal coil design satisfying the required design parameters and showing the feasibility of the proposed model into real-world clinical applications. The following steps are followed throughout this work:

- Choose and modify a surface RF coil model that is expected to meet the requirements.

- Determine the essential parameters that would affect the performance of the

proposed coil by performing parameter study through simulations.

- Find mathematical relationships between design parameters and coil characteristics and define the optimal design for the pituitary gland imaging application.

- Validate the proposed coil designs through phantom experiments for future works.

2. Background

In this section, we will discuss the fundamentals of the MRI system and the physics behind it. The first two subsections are organized based on first and third chapters of [7], and the third subsection will discuss some design parameters that are important in terms of coil performance, followed by a brief introduction to some coil design examples.

2.1. MRI System

A typical clinical MRI scanner has three main hardware components, including a main (static) magnet, a magnetic field gradient system, and an RF system [7]. More specifically, an MRI system can be further categorized into the following major hardware components: main magnet, RF coil, gradient coils, RF pulse transmitter, RF receiver, data acquisition system, power supplies, and cooling systems [16].

2.1.1. The Main Magnet

The *main magnet* provides a strong uniform static field, used for the polarization of nuclear spins in an object [7]. This field is also referred to as the B_0 field. The *spatial homogeneity* describes the uniformity of the main magnet field. To obtain a clear image, it is important to maintain a moderate homogeneity over a relatively large volume in the center of an MRI scanner [17]. However, in practice, the main magnet alone has limited capability of generating such a highly uniformed distributed field. A set of shim coils can then be employed to generate designed patterns of magnetic fields, eliminating harmonic components [18] and thus obtaining the required spatial homogeneity.

2.1.2. The Gradient System

The *gradient system* is used to artificially generate controlled spatial non-uniformity [7]. It has the functionality of providing the required spatial encoding. The gradient system normally consists of three orthogonal gradient coils [7], i.e., X-Gradient, Y-Gradient and Z-Gradient. These gradient coils will be responsible for generating gradient fields with components that vary linearly along the x-, y-, and z- directions, respectively [19], [20]. The Maxwell coil is a pair of coils separated by 1.73 times radius and fed with currents in opposite directions, and it can be used to generate gradient field. A saddle coil is represented by at least four conductors (called rungs or rods) placing on top of a circular cylinder, forming a saddle shape [21]. Normally, the Maxwell coil pair is used to establish the z-gradient, while saddle coils are used to construct x- and y- gradients (also called the transverse gradients). Key factors for measuring the performance of a gradient system include the *peak gradient strength* and the *rise time*. Rise time is defined as the time required for the gradient to reach peak strength. The two factors can be combined in the *slew rate*, which is defined as the peak gradient strength divided by the rise time [19].

2.1.3. The RF System

A typical *RF system* consists of two types of coils, i.e., transmitter coils and receiver coils. The *transmitter coil* is responsible for the generation of a rotating magnetic field that excites a spin system transversally. This rotating magnetic field is also referred to as the B_1 field [7]. On the other hand, the *receiver coil* converts a precessing magnetization into an electrical

signal, delivering information from the target through spin processing and then further transforming the information into human-readable images through data processing [7]. The single loop coil is the simplest form of a receiver surface coil. When using this coil, magnetic flux variations within the region will induce a small current containing information about the inner structure of the sample within the coil according to Faraday's Law [22]–[24]. This current is then analyzed to extract information. The *transceiver coil* is a single coil used as both transmitter and receiver. The coil can be switched from the transmit mode to the receive mode after a RF transmission [22].

2.2. MRI Physics

Atoms with odd atomic weights have *nuclear spins* [25]. The ensemble of nuclei of the same type in the target object to be imaged is called a *nuclear spin system* [7]. The *nuclear magnetism* of a nuclear spin system in the presence of an external magnetic field forms the fundamental basis of MRI [7].

2.2.1. Nuclear Magnetic Moments

The *nuclear magnetic dipole moment* or *magnetic moment* $\vec{\mu}$ is related to the spin angular momentum $\vec{J}$ by the relationship

$$\vec{\mu} = \gamma \vec{J} \qquad (2.2.1.1)$$

where γ is the *gyromagnetic ratio*. The value of the gyromagnetic radio depends on the property of nucleus. Although the magnitude of $\vec{\mu}$ remains the same (with or without the external magnetic field), thermal random motion will keep its direction in a complete random

state if no external magnetic field is presented [7]. To form magnetism in the macroscale, at least a small proportion of the spin vectors should be lined up. This can be done by applying a strong external magnetic field. Assume an external field with magnitude B_0 is applied in the z-direction in the laboratory frame [7],

$$\vec{B_0} = B_0\vec{k} \tag{2.2.1.2}$$

where we define $\vec{\imath}$, $\vec{\jmath}$, and $\vec{k}$ to be the unit directional vectors along the x-, y-, and z-axes, respectively. Then, in a spin-$\frac{1}{2}$ system, any magnetic moment vectors can only be aligned in two directions, i.e., either parallel ("spin-up state") or antiparallel ("spin-down" state) to the direction of applied external field [7].
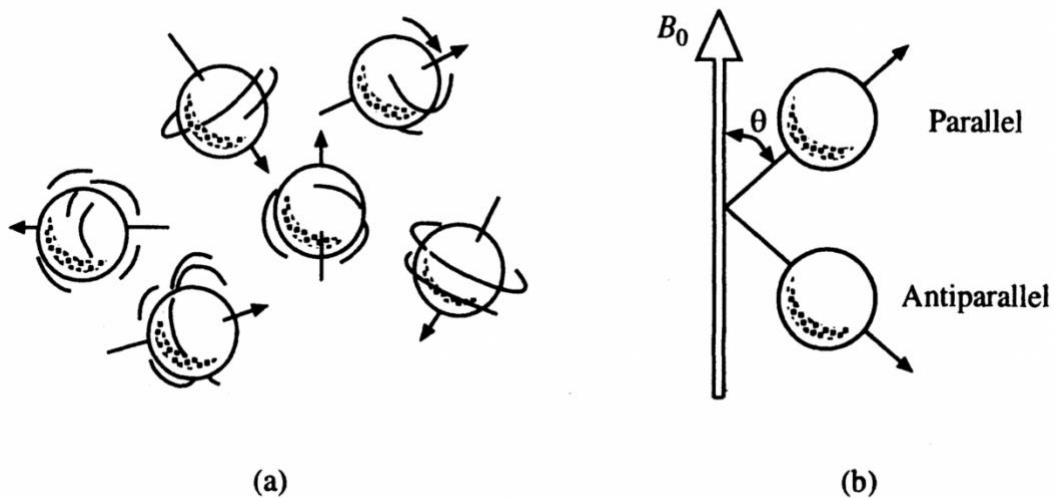
Figure 2.1 Magnetic moment (a) in random directions due to random thermal motions and (b) in parallel and antiparallel directions when exposed to external magnetic fields [7].

Precession describes the slow circular movement of the axis of a spinning object around another axis. *Nuclear precession* is defined as the precession of the magnetic moment around the direction of the external field. The angular frequency of the nuclear precession around the z-direction is also known as the *Larmor frequency*. The relationship between the magnitude

of the Larmor frequency w_0 and the magnitude of the main field B_0 is called the Larmor equation.

$$w_0 = \gamma B_0 \qquad (2.2.1.3)$$
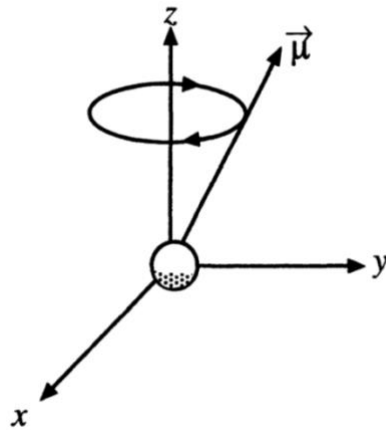
Figure 2.2 Nuclear precession showing the circular movement of the axis of magnetic momentum around z-direction [7].

Combining all the microscopic magnetic momentum vectors of the object together, we have the *macroscopic magnetization vector* $\vec{M}$.

2.2.2. RF Excitation, Free Precession, and Relaxation

By Planck's law, electromagnetic waves with frequency w_{rf} carries energy

$$E_{\text{rf}} = \hbar w_{\text{rf}} \qquad (2.2.1.4)$$

Coherent transition from one spin state to another will only take place when the energy gap between the two states is equal to the energy delivered by the electromagnetic wave. Hence, we have the *resonance condition*. It states that the frequency of the electromagnetic radiation should be equal to the Larmor frequency.

$$w_{\text{rf}} = w_0 \qquad (2.2.1.5)$$

A standard RF pulse, or B_1 field is given by

$$B_1(t) = B_{1,x}(t) + iB_{1,y}(t) = B_1^e(t)e^{-i(w_{rf}t+\varphi)} \qquad (2.2.1.6)$$

where $B_1^e(t)$ is the pulse envelope function, w_{rf} is the excitation carrier frequency, and φ is the initial phase angle [7]. In general, the generated $\overrightarrow{B_1(t)}$ oscillates in a direction that is perpendicular to the main field $\overrightarrow{B_0}$. Mathematical analysis with Bloch equation shows that if RF pulse excitation is on-resonance, it will induce a precession of the macroscopic (bulk) magnetization vector around the x'-axis in the RF-rotating frame defined by

$$\vec{i}' \triangleq \cos(wt)\vec{i} - \sin(wt)\vec{j}$$

$$\vec{j}' \triangleq \sin(wt)\vec{i} + \cos(wt)\vec{j} \qquad (2.2.1.7)$$

$$\vec{k}' \triangleq \vec{k}$$

This precession of $\vec{M}$ around the B_1 field is also referred to as the *forced precession*. After the process of forced precession, the macroscopic magnetization vector is pushed (flipped) away from the z'-axis, leading to an observable transverse component $\vec{M}_{x'y'}$ [7]. The *flip angle* is defined as the angle between $\vec{M}$ and the z-axis. By the end of an RF pulse, the magnitude of the flip angle can be calculated by

$$\alpha = \int_0^{\tau_p} \gamma B_1^e(t)dt \qquad (2.2.1.8)$$

where τ_p is the input pulse width.

The system will return to thermal equilibrium state after the RF perturbation is eliminated, which is realized through the precession of $\vec{M}$ around the B_0 field. This precession process is called *free precession*. The process through which the transverse magnetization M_{xy} decays is

referred to as *transverse relaxation*. Accordingly, the reconstruction of the longitudinal

magnetization M_z is named *longitudinal magnetization*. The mathematical formulations of

both magnetizations are given by [7]:

$$M_{x'y'}(t) = M_{x'y'}(0_+)e^{-t/T_2}$$

$$M_{z'}(t) = M_z^0(1 - e^{-t/T_1}) + M_{z'}(0_+)e^{-t/T_1}$$

(2.2.1.9)

where $M_{x'y'}(0_+)$ and $M_{z'}(0_+)$ are defined as the magnitude of the macroscopic

magnetization on the transverse (*xy-*) plane and along the *z*-axis at the instant after the

termination of the RF perturbation, respectively [7]. In this formulation, T_1 is the *longitudinal*

relaxation time constant, and T_2 is the *transverse relaxation time constant* [26].

2.2.3. Signal Detection

According to the Faraday law of induction, the raw NMR signal $V(t)$ induced in the receiver

coil can be expressed by

$$V(t) = -\frac{\partial}{\partial t}\int_{\text{object}} \vec{B}_r(r) \cdot \vec{M}(r,t)dr$$

(2.2.1.10)

where $\vec{B}_r(r)$ is the magnetic field at position *r* induced by a hypothetical unit direct current

in the perspective of the laboratory frame, and $\vec{M}(r,\text{t})$ is the magnetic flux through the coil

[7].

2.3. MRI Coils

2.3.1. Transmitter Coils and Specific Absorption Rate (SAR)

The main purpose of transmitter coils is to generate a homogeneous B_1^+-field and minimize

the transient time of bulk magnetization from the equilibrium state to its peak value [5]. As

mentioned in equation (2.2.1.8), the magnitude of the flip angle will be determined by the gyromagnetic ratio, the B_1 field, and the duration of the perturbation. From this, the magnitude of the transmitted field B_1 will depend on the power delivered by the RF amplifier and the properties of the selected RF coil.

Here we focus on the resonators that create a homogeneous oscillating magnetic field within the sample volume and these resonators can be categorized into the axial resonators and transverse resonators [27]. They produce homogeneous RF fields, as required. Axial resonators generate magnetic fields along their symmetry axis whereas transverse resonators create magnetic fields perpendicular to their symmetry axis [27]. For axial resonators, the ideal spherical geometry (with a sinusoidal current density on the surface of a sphere) can be approximated by two coils (the Helmholtz) and four coils (the Hoult-Deslauriers) designs [27], [28]. The ideal cylindrical geometry (a cylinder of infinite length) is approximated by the solenoid coil [5], [27]. For transverse resonators, the basic approximation of the cosine-dependent distribution of linear currents flowing in a direction that is parallel to the cylindrical axis gives rise to a geometry known as a "saddle coil" [5], [29]. Another example of transverse resonator that mimics the ideal current cosine distribution around the cylinder is the "birdcage", which is basically constituted of identical resonators evenly distributed around a cylinder [27]. Combined, the axial loop-gap (single-turn solenoid coil) and the transverse birdcage resonators can achieve the best homogeneity [27], [30].

On the other hand, RF transmitter coils also pose the threat of heating to the target tissues. Alternating electromagnetic waves can induce conduction currents inside the tissues, and the

energy absorbed by the target tissues is described by the *specific energy absorption rate* (SAR) [31]. There are regulations regarding the safety issues related to MR systems [32], [33]. In general, an unexpected rise in tissue temperature may cause severe damage to certain patients, including, for example, patients with reduced thermoregulatory capacities, difficulties in sensing or communicating heat sensations, extensive tattoos, implanted organs or devices, and many other conditions [34]. However, safer approaches that reduce SAR will mostly come at the expense of reduced image quality. For instance, when gradually reducing the phase reversal pulse from 180 to 90 degrees, the average SAR (W/kg) decreases, but at the same time, the signal also decreases due to the incomplete rephasing of the spins in the X-Y plane [35].

2.3.2. Receiver Coils, Signal-to-Noise Ratio (SNR) and Other Factors

A simple interpretation of a basic receiver coil is a LC circuit tuned to the resonance frequency:

$$w_r = \frac{1}{\sqrt{LC}} \qquad (2.2.1.11)$$

where w_r is the angular resonance frequency. L and C are the inductance and capacitance, respectively.

One of the preliminary goals of the receiver coils is to achieve the highest SNR if possible. In MRI, the SNR is calculated based on a comparison between strength of the signal obtained from the ROI and the background noise. The difference between the actual signal and the background noise can be further divided by the standard deviation of the background noise. In [36], several methods have been investigated to increase the SNR, and these attempts

include: (1) adopting volume acquisition at the expense of increasing imaging time; (2) using spin-echo sequences; (3) decreasing the noise by reducing the bandwidth, using surface coils, and increasing the number of excitations; (4) increasing the signal by decreasing the *time to echo* (TE) and increasing the *time to repeat* (TR), slice thickness, or *field of view* (FOV).

The intrinsic SNR (ISNR) is the upper limit of detectable and achievable SNR given the fact that the performance (i.e., detection efficiency and noise) of elements on the receiver chain will potentially degrade the SNR [37]. In [38] and [24], the formula to calculate ISNR is given by

$$\text{ISNR} = \frac{V_{\text{sig}}}{V_{\text{noise}}} = \frac{w \Delta V M_0 |B_t^-|}{\sqrt{4kT\Delta f R_L}} \tag{2.2.1.11}$$

where V_{sig} and V_{noise} are the peak signal and the standard deviation of the background noise, respectively. w is the Larmor frequency, ΔV is the volume of the voxel, M_0 is the magnitude of the macroscopic magnetization, $|B_t^-|$ is the magnitude of the left-hand circular polarized component of the transverse RF field induced by the standard current in the coil, k is the Boltzmann's constant, T is the absolute temperature, Δf is the bandwidth of the receiver, R_L is the resistive loss of the system when the coil is loaded with the sample, which can be summarized into three main sources, i.e., coil loss, sample loss, and electronics loss. Based on formula (2.2.1.11), we can use $|B_t^-|$ as an approximation to the ISNR, when the variations in other factors are negligible.

Other factors can also play important roles in determining the achievable SNR. The quality factor Q is defined as the ratio of the energy store and dissipated. It can be further calculated

by the maximum energy stored in the loop divided by the average energy dissipated per cycle [5]. The formula is to calculate Q for the resonance circuit in a loop is given by

$$Q = \frac{wL}{R} \tag{2.2.1.12}$$

where L is the inductance and R is the overall equivalent resistance of the loop.

The relationship between the quality factor Q and the SNR is given [39] by

$$\text{SNR} \propto B_0^{7/4} \cdot \sqrt{Q/T_\text{P}} \tag{2.2.1.12}$$

where B_0 is the main magnetic field, T_P is the temperature of operation. From the equation we may see that increasing the main magnetic field can significantly improve the SNR. An increment in the quality factor can also improve the performance of the system, and this improvement can be more significant for MRI systems operating under low magnetic fields since B_0 is raised to the power of $\frac{7}{4}$ in the formula.

In equation (2.2.1.12), if the overall loss is considered when evaluating the R term, we will obtain Q_Loaded. If the sample loss is excluded from the evaluation of the R term, the resulting Q is defined as Q_Unloaded. The coil sensitivity can be inferred from the ratio between the unloaded quality factor and the loaded one, and this ratio can be further approximated by the sum of coil loss and sample loss divided by the coil loss. If the coil is operating in a regime dominated by coil loss, attempts to minimize the coil loss can improve the SNR [5]. However, in many cases [39], the operation mode where sample noise dominates is an indicator of a good design [5], and in this situation, improving the quality factor will not cause a significant increase in the SNR.

The *filling factor* is defined as the ratio of the magnetic field energy stored inside the sample volume versus the total magnetic energy stored by the RF coil and it provides a measurement of the geometrical correspondence between the RF coil and the sample [40]. This indicates that fitting the coil closer to the region of interests can effectively improve the filling factor [40]. A filling factor close to one gives the highest SNR.

2.3.3. Single Loop Coils, Figure 8-Shaped Coils and Other Coils

Single Loop Coils are the simplest forms of RF coils. They are usually formed by a single loop of wire. Due to the close coupling of the nuclei in ROI to the surface coil itself, these coils can achieve high SNR for surface structure detection [41]. The optimal radius r_0 is known from numerical and theoretical analyses in the low-field limit [24]

$$r_0 = \frac{d}{\sqrt{5}}$$
(2.2.1.12)

where *d* is the desired target depth.

Figure 8-shaped coils can have the standard circular shape, as shown in the figure below. The design rule of which is defined based on a linear line fit to the full-wave analysis data and the Bio-Savart method [24], and the optimal radius r_8 for target depth *d* is given by the formula

$$r_8 \approx 0.6d$$
(2.2.1.12)
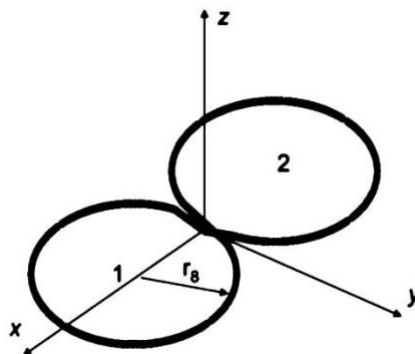
Figure 2.3 Idea figure 8-shaped coil. The quadrature coils should be placed in a direction orthogonal to that of the main magnetic field [24].

Figure 8-shaped coils can also be in square form. In [24], when placing the figure 8-shaped coil with a circular loop as in the common quadrature configuration, the design rule is stated, in which the radius of the ideal figure 8-shaped coil should be about 1.34 times that of the circular loop one, and the side length of the square-shaped figure 8 coil should be about twice the radius of its circular loop counterpart. These results are based on numerical EM calculations.

However, due to the difficulty of fitting large coils into the cavity above our target ROI, in this study, we adopt and study the following figure 8-shaped coil, as shown in the right side of the figure below. More detailed reasons of selecting a circular figure 8-shaped coil with two linear elements in series over a standard circular loop coil will be discussed in later sections.
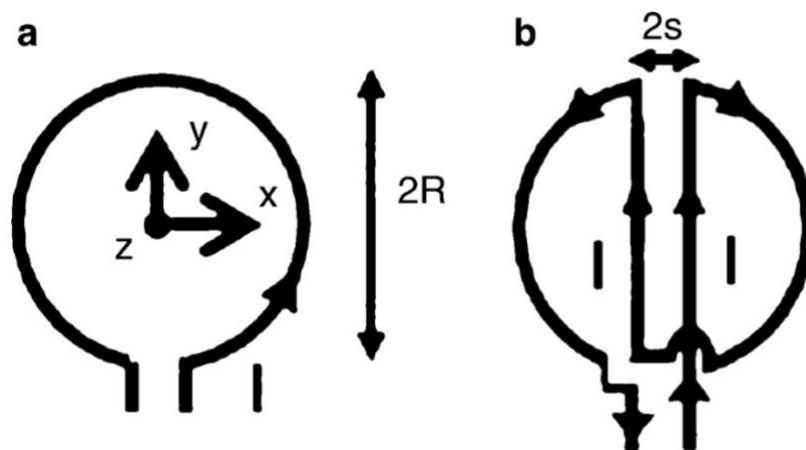
Figure 2.4 Schematic diagram of the: **a** standard RF single loop (CL) surface coil; **b** circular figure 8-shaped surface coil with two linear elements in series connection [6].

17

3. Materials and Methods

In this section, we will discuss the optimal design for circular figure 8-shaped surface coils with two linear elements connected in series (Fig. 2.4b). COMSOL Multiphysics (COMSOLAB, Stockholm, Sweden) based simulations will find the optimal distance (namely, $2s$, in the Fig. 2.4) between the two linear elements in parallel, the optimal radius r for the circular-8 shape coil given a target depth d, and finally the image quality variation in the presence of coil rotation.

The coil itself can be simulated by four evenly distributed capacitors and an inductor connected by perfect electric conductors in COMSOL. A uniform excitation is applied through the lumped port.

The size of the mesh grid should be carefully selected. Small mesh sizes can improve the accuracy and stability of the results. However, if the mesh size is too small, the computation time per iteration will increase dramatically, but the smoothness and stability are not significantly improved, leading to an unnecessary increase in the cost.

The boundary conditions are selected to be scattering to address the unintended behaviors of the system resulting from an unexpected number of electromagnetic waves reflected from the boundaries.
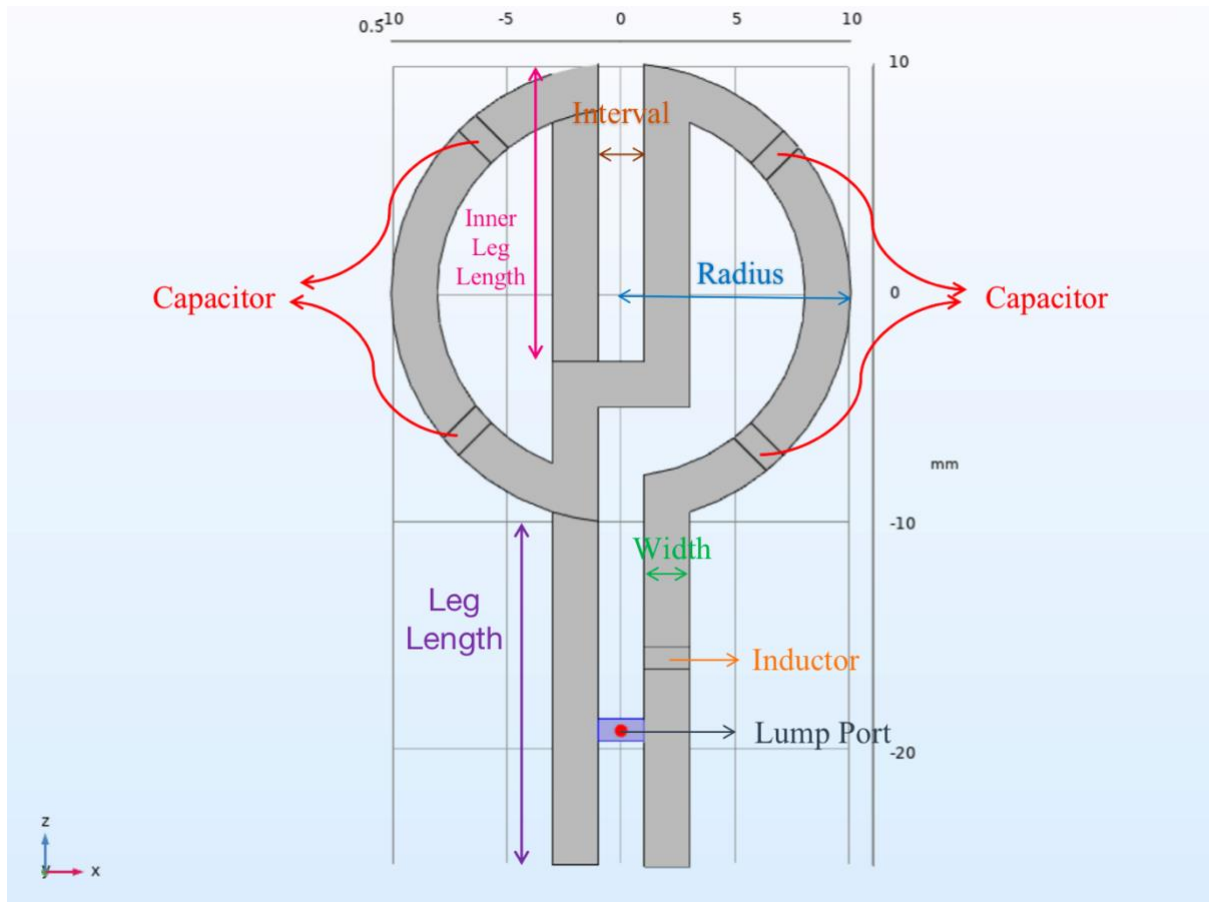
Figure 3.1 *xz*-plane view of the circular figure-8 coil structure, where the interval and radius are marked up. There are four capacitors evenly distributed on the loop and there is also an inductor located on one of the legs. These two lumped elements are used for *tuning*. The lumped port is uniformly excited with a characteristic impedance adjusted for *matching*. The width *w* is 2 mm. The leg length l_1 is 16 mm. The inner leg length l_2 is 1.5 times the radius. The height between the two layers is 1 mm. The magnitude of other parameters may subject to change in different designs. For example, in the design with a radius of 10 mm and an interval of 2 mm, the inner leg length l_2 is 15 mm.

When the external excitation is applied, current flows in the conductors, generating a

magnetic field distribution. In Fig. 3.2, the magnetic field direction is indicated by the arrows.

We may see that the field distributions in the direction that is perpendicular to the coil plane

cancel out, leaving the main field distribution of the circular figure-8 coil parallel to the coil

plane, which can be visualized from the thickened arrow in the horizontal direction.
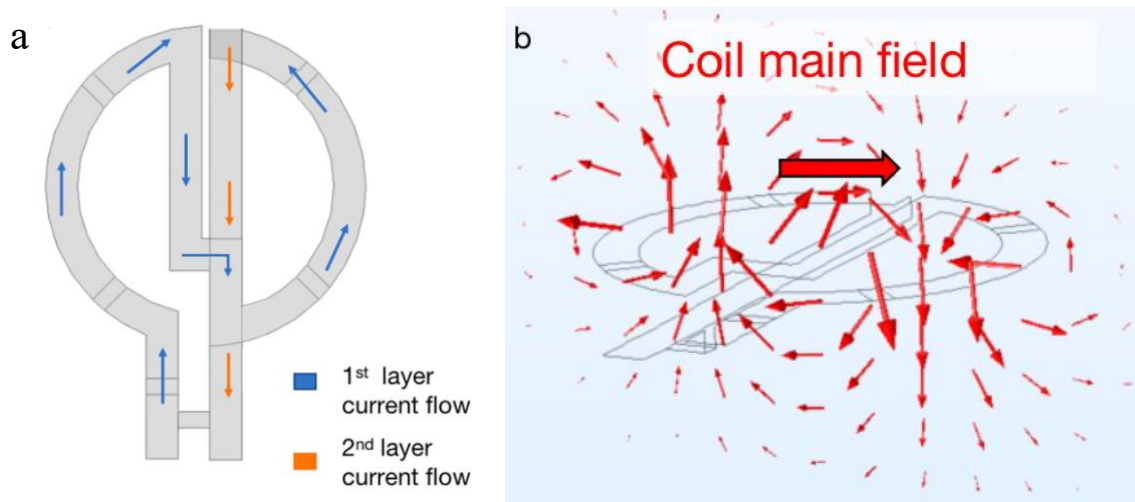
Figure 3.2 a Current flow directions in the upper and lower layer; **b** Main magnetic field distribution of circular figure-8 coil.

The ROI is approximated by a 10 mm diameter, 3 mm thickness cylinder place 10 mm below the coil plane, shown in Fig. 3.3. This ROI corresponds roughly to the pituitary gland region to be imaged.
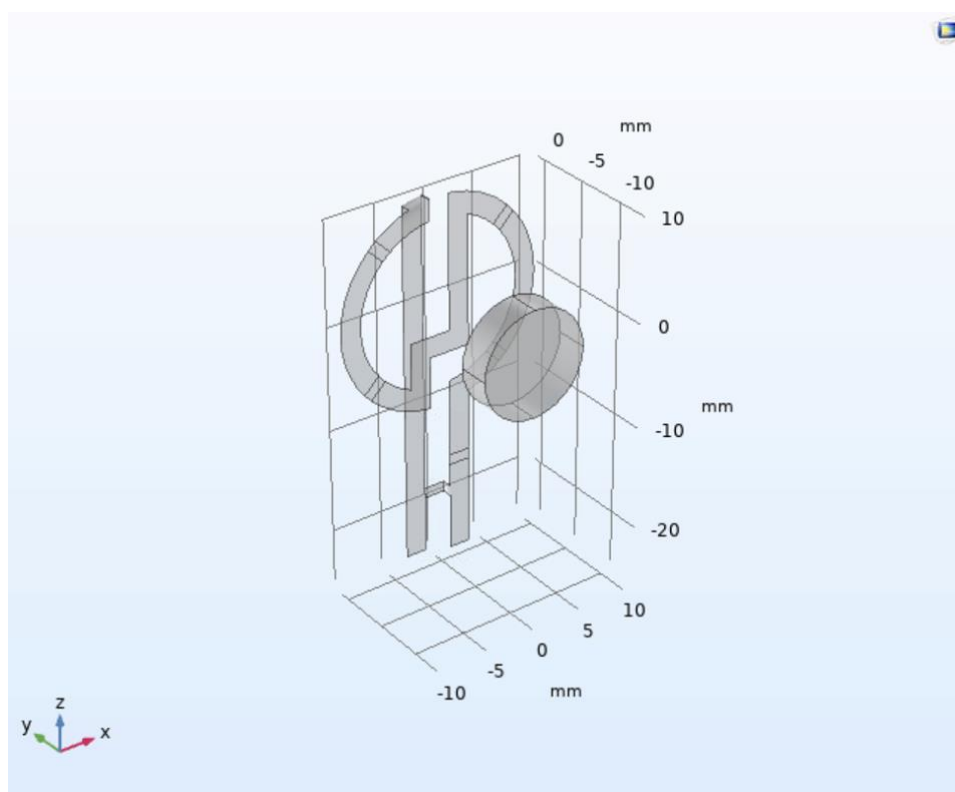
Figure 3.3 The coil is placed 10 mm above the target region of interest. The overall $70\text{mm} \times 70\text{mm} \times 40\text{mm}$

20

phantom with scattering boundary conditions is not shown in the graph.

To determine capacitance and inductance, a parameter sweep is performed. In this process, the inductance is fixed to 20 nH, and the capacitance is swept in the frequency domain of 123.2 MHz (corresponding to 3 Tesla MRI). The input impedance of the lumped port is also adjusted, simulating the process of matching, so that the desired S11 (reflection coefficient) is achieved.
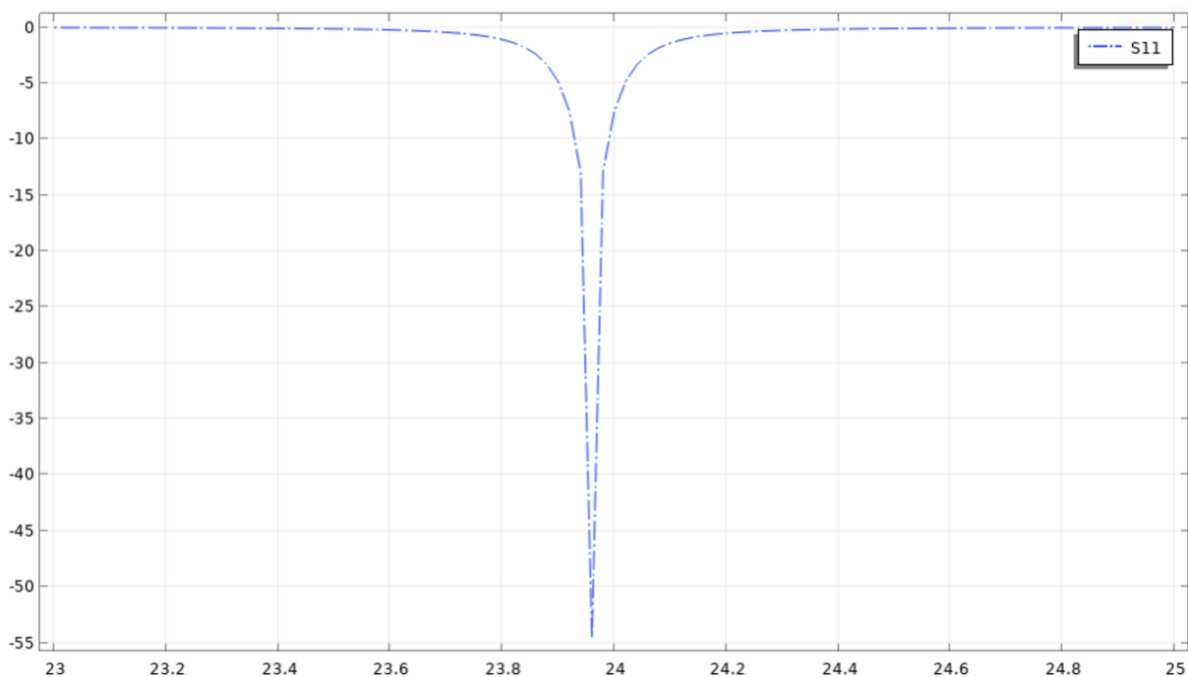
Figure 3.4 Sample parameter sweep results. The x-axis is the capacitance in pF, swept in a step of 0.02 pF. The y-axis is the S-parameter (S11) in dB. The minimum value of -54.48 dB is achieved when the capacitance is set to 23.96 pF and the input impedance is matched to 0.096 Ω.

3.1. Study of Intervals

Recall that in Fig. 3.1, the *interval* is defined as the distance between the two legs of the coil or equivalently, the distance between the two semicircle-shaped components. The list of intervals to be investigated includes 1mm, 2 mm, 4 mm, 6 mm, 8 mm, and 10 mm. In each

design, we only adjust the length of the interval between the two parallel sides of the linear components in series while keeping the radius fixed. All the coils are tuned to the resonance frequency (123.2 MHz). For each selected interval, we will look at the performance of the model by examining the field distribution in a range from 0 mm to 20 mm below the coil plane. For each integral value of the depth in this range (0 mm-20 mm), we will consider the average field and the maximum field for a 10 mm diameter, 1 mm thickness slice in the shape of a cylinder. The average field is plotted for different depth, and the resulted lines from different interval are aligned together for comparison. The maximum field is also plotted and compared as a reference. From here, the optimal interval length can be determined.

3.2. Study of Radius

In this study, we discretize the continuous depth from 0 mm to 90 mm with a step of 1 mm and analyze the optimal radius for each of these integral target depths. Models of radius range from 8 mm to 50 mm, with a step of 2 mm, are built and carefully tuned.

In each model with radius r, we take out the magnitude of the effective field on the axis and perform a floor operation on the depth. For a given input, the floor operation gives the greatest integer less than or equal to the input. In our case, for each integer depth n, we find the maximum field in interval [n, n+1] and record it.

We do the similar for each coil model so that the maximum field of each coil at depth n is determined. To find the optimal radius for a given target depth, we compare the field of all coils at the same depth, and the one that gives the maximum field among all has the optimal radius for this depth.

We will then plot the optimal radius against the target depth and perform a linear regression on the obtained data, the design rule to determine the radius for the circular figure 8-shaped surface coil shall be determined.

In the study of the optimal interval length and the optimal radius for a given target depth, the rotation angle is assumed to be 0 degrees. In other words, the coil is assumed to be placed in parallel with the top of the target block.

3.3. Study of Rotation Angles

The effects of rotation have been studied in the case of single loop coil design for the clinical application of pituitary imaging [4]. Given the fact that figure-8 coils in general present good resistance to the rotation angle variations (~20% drops in 90 degrees compared to 0 degree in the same ROI [6]), we carefully select a variation of circular-shaped figure-8 coil that accommodates the high-SNR requirement of pituitary imaging at various angles. The definition of rotation angle utilized in this study is illustrated in Fig. 3.5.
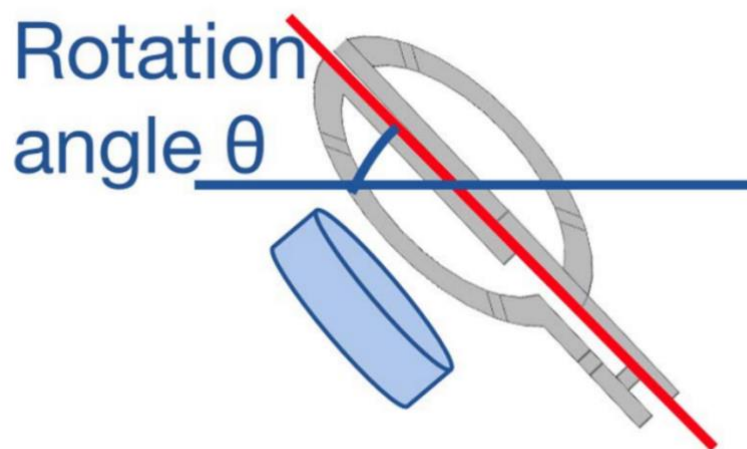
Figure 3.5 A figure illustrating the *rotation angle*. The red line is indicating the axis of the coil plane and the horizontal blue line is on the direction of the main field. The rotation angle is defined as the smaller angle between these two indicator lines.

The formula to calculate the effective field is given in [4], shown in Eqn. (3.3.1).

$$B_{1y\,effective} = B_{1y} \cdot cos\theta - B_{1z} \cdot sin\theta$$

$$B_{1xy\,effective} = \sqrt{B_{1x}B_{1x}^* + B_{1y\,effective}B_{1y\,effective}^*}$$

(3.3.1)

where θ is the rotation angle, and the B_{1x}, B_{1y}, and B_{1z} are the *x*, *y*, and *z* component of the received magnetic fields at 0 degrees, respectively. In Fig. 3.3, the coordinate system is defined, and it shows the case for 0-degree rotation where the coil is placed in the xz-plane, and the orthogonal coil axis (i.e., the axis orthogonal to the coil plane) is in the y-direction. The rotation angle is defined to be the angle between the coil plane and the z-axis, and for 90-degree rotation case, the coil is placed in the xy-plane with the axis orthogonal to the coil align with the z-direction. The three *B* components remain constant in the effective field calculation during the rotation.

The effective field for angles in the ranges from 0 to 90 degrees with a step of 1 degree is calculated for the model with 10 mm radius and 2 mm interval distance. The resulting effective fields are plotted against the angle to demonstrate the rotation angle related performance of figure-8 coil in our application.

3.4. Study of SAR and Temperature Variations

The basic head geometry employed here is the simplified physical model (phantom) of the human head specified in IEEE 1528 and IEC 62209-1, the specific anthropomorphic

mannequin (SAM) [42]. The material parameters within the model are sampled by a volumetric interpolation function that estimates the tissue variations within the head based on MRI measurements originally performed by University of North Carolina and the version adopted here can be found at the Stanford volume data archive [43].

To accommodate for our application, we include a brain area, a pituitary gland, and a cavity to simulate the clinical environment of the coil. The figure 8-shaped coil is placed in front of the pituitary gland and inside the cavity. The size of the cavity is based on the average of clinical measurements, with a height of 24 mm, a width of 27 mm and a depth of 12 mm. The maximum dimensions of the cavity can be approximated by a height of 33 mm, a width of 38 mm and a depth of 15 mm. The cavity used in simulation can hold the coil properly, as shown in the figure below.
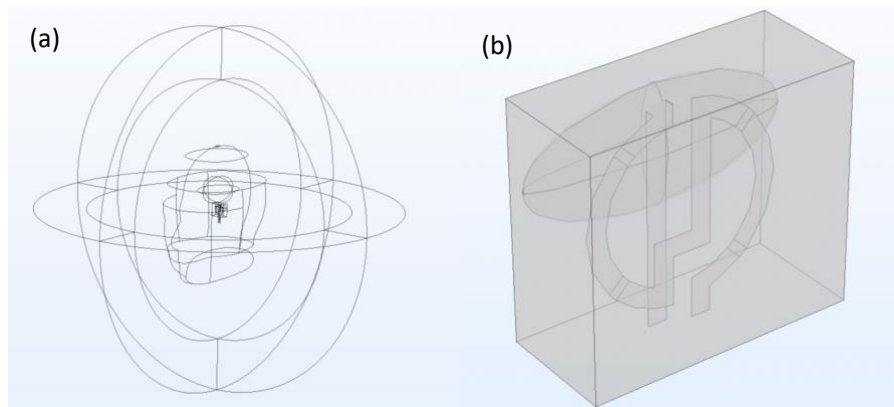
Figure 3.6 (a) Model overview. Scattering boundary condition is applied to the outside sphere. The bioheat transfer model is applied to the human head region. **(b)** A schematic view of the placement of the figure 8 shaped coil inside the cavity.

Material	Relative Permittivity	Relative permeability	Electrical conductivity S/m	Density kg/m^3	Thermal conductivity W/(m-K)	Heat capacity at constant pressure J/(kg-K)
Brain	54.7	1	2.09	1000	0.51	3630

Table 3.1 Parameters used for the brain section modeling.

The limits of the SAR averaged over the whole body recommended by the National Radiological Protection Board (NRPB) are 1 W/kg for periods more than 30 min, 2 W/kg for periods shorter than 15 min, and 30 W min/kg for periods of intermediate duration [44]. The local SAR is defined as an average over 1 kg tissue for a period of 6 min. For the head, the local SAR limitation is 2 W/kg [44]. In terms of temperature variations, the physical limit of the temperature increments in the brain for severe physical damage is approximately 3.5 degrees [45]. However, temperature increments as small as 0.2 degrees can alter the thermoregulatory behavior in the hypothalamus [45].

The coil is excited by a 1V lump port (voltage source), and capacitance, inductance, and input impedance are adjusted so that the coil is tuned and matched to 123.2 MHz to simulate the 3 T environment. The local SAR distribution and temperature variation in the pituitary region and the brain will be studied. Slices and volume plots for temperature variation and SAR distribution in the corresponding regions will also be generated to provide a better visualization.

4. Results

For the 10 mm radius model, the average and maximum field distributions for six intervals are simulated and evaluated. From Fig. 4.1 we can see that the 1 mm-interval model and the 2 mm-interval model have the largest average and maximum field distributions among all the models. However, the improvement of the effective field's magnitude from the 2 mm-interval model to the 1 mm-interval one is not very significant. If we look at the depth between 10 mm and 13 mm (the estimated depth range of ROI), the effective field's magnitude increases by 85.5115% on average if the interval decreases from 10 mm to 2 mm. However, the effective field's magnitude only increases by < 2.6995% on average if the interval decreases further below 2 mm. Hence, we conclude that the optimal interval is $\leq$ 2 mm. For the following simulations, we select 2 mm as a representative of optimal intervals.

(a)

(b)
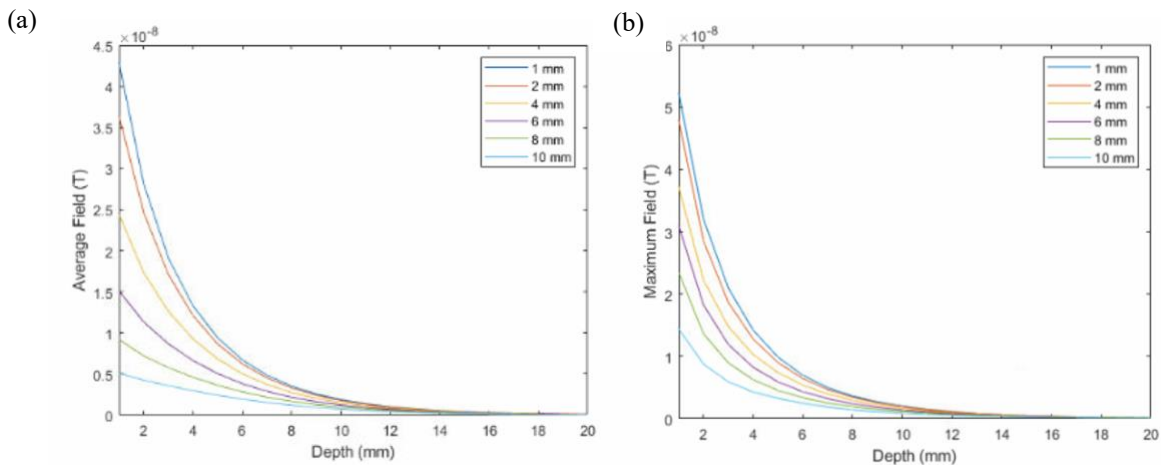
Figure 4.1 (a) Average field distribution and **(b)** maximum field distribution in a 10 mm-diameter, 1 mm-thickness cylinder placed in depth between 0 mm and 20 mm below the coil plane. Intervals 1 mm, 2 mm, 4 mm, 6 mm, 8 mm, and 10 mm are evaluated, and the optimal interval is determined to be $\leq$ 2 mm. We select 2 mm (in the optimal range) for the following simulations.

After constructing models with radius range from 8 mm to 50 mm (with a step of 2 mm), the optimal radius for each target depth is determined and plotted against the target depth. We

may see that the data points distribute linearly. By performing linear regression on the

obtained data, we construct a linear model

$$r = 0.53348d + 1.7747 \tag{4.1}$$

where r is the radius (mm), and d is the target depth (mm). Typically, the allowed coil

diameter for the pituitary measurement is between 10 mm and 35 mm (with median 26.8

mm), and the target depth is between 5.8 mm and 14.8 mm (with median 8.7 mm). From the

plot, we can observe that a coil design with radius 10 mm can cover the required target depth

and fit into the cavity above the target object.
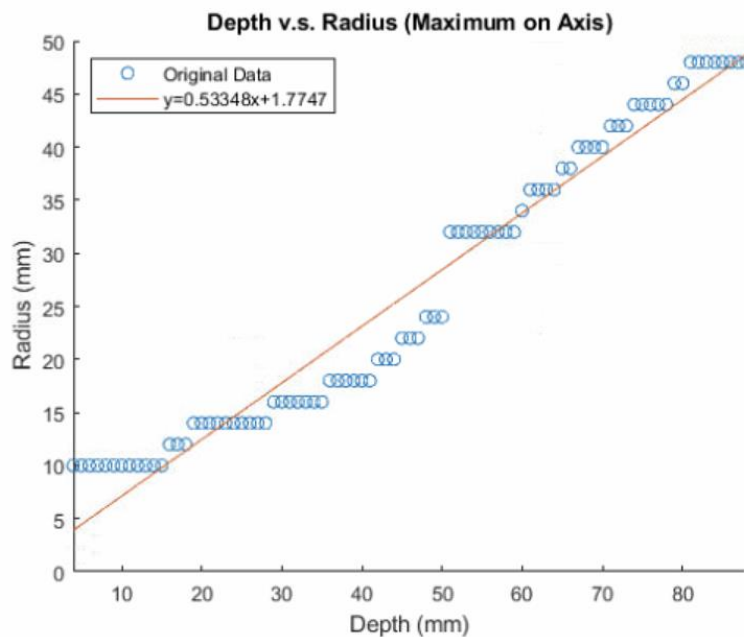
Figure 4.2 Optimal radius plotted against target depth. Each optimal radius is selected in a way such that it generates the maximum field distribution for a given target depth. The result is quantized due to the floor operation performed on the input depth so that the fields within range [n, n+1] are boxed together for integer depth n. Based on the plot, we can see that for target depth between 5.8 mm and 14.8 mm, a radius selection of 10 mm is suitable.

For the 10 mm-radius, 2 mm-interval model, the effective field distribution for a circular-

shaped surface with diameter 10 mm located 10 mm below the coil plane is plotted for both

single loop coil design and its circular figure 8-shaped counterpart at different angles (0, 30, 60, and 90 degrees). The circular figure 8-shaped butterfly coil is tuned to a S11 below -30dB, and the same excitation is applied to the single loop coil design. From the plot, we can see that the single loop coil design will have a "dead spot" in the center of the target surface when rotated 90 degrees. However, at 90 degrees, the circular figure 8-shaped coil will still have a field strength at the center of the target surface close to the 0-degree rotation case.
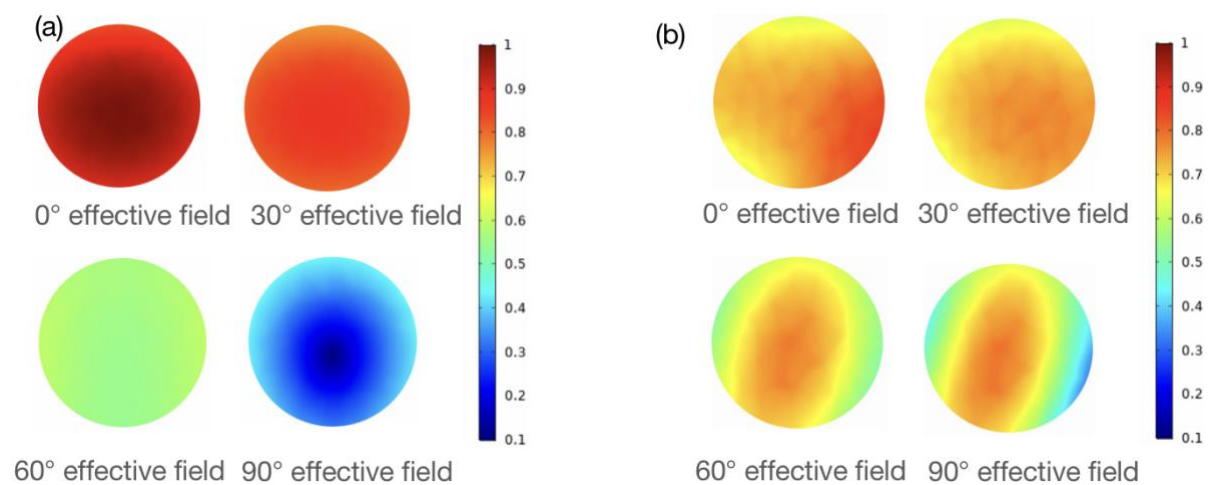
Figure 4.3 Effective field distribution at 0, 30, 60, and 90 degrees for **(a)** single loop coil and **(b)** circular figure 8-shaped coil. All the presented field distributions are normalized by the maximum field for single loop coil at 0 degree for better comparison. For single loop coil, although the maximum field at 0 degree exceeds that of its figure-8 counterpart, the average field drops significantly when the rotation angle increases. Also, at 90 degrees, a clear dark blue "dead spot" shows up in the center, blurring the obtained image. However, for figure 8-shaped coil, the field distribution near the center remains almost the same under rotation, eliminating the potential danger of a "dead spot". Note that larger coils still suffer from the "dead spot" problem, and they are harder to fit into the small cavity near the ROI.

Apart from the issue of "dead spot", the average field distribution within the ROI at 90 degrees drops to a value around 30% of the average field distribution at 0 degree. In the contrary, the average field distribution of figure 8-shaped coil remains almost consistent (~70%) with respect to angle deviations. As a result, we will experience a less significant SNR drop at 90 degrees for the latter case. We can see that there is a trade-off between

maximum field generation and "dead spot" elimination (SNR improvement at all angles).

This property was first studied in [37].
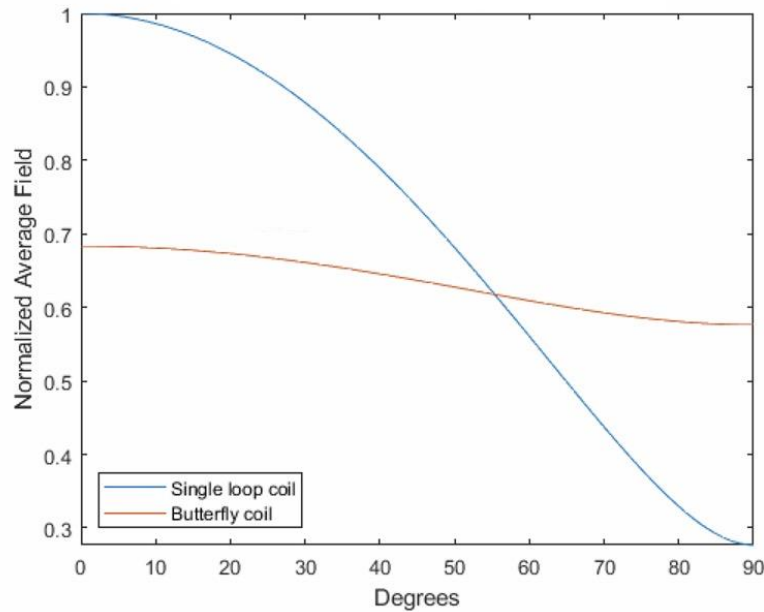
Figure 4.4 Normalized average field distribution for single loop coil and for butterfly coil. All the values are normalized by the maximum value for single loop coil (at 0 degrees). For single loop coil, the minimum value 0.2767 is achieved at 90 degrees. For figure 8-shaped coil, the maximum value 0.6834 and the minimum value 0.5764 are obtained at 0 and 90 degrees respectively, examining the differences.

Another interesting aspect to be studied is the trade-off between angle deviation and spatial

shifts. A *shift* is defined when the object is not placed perfectly below the center of the coil,

and its magnitude is defined as the deviation of the target object from the center of the coil

along the coil axis. A 10 mm-diameter, 3 mm-thickness cylinder placed 10 mm below the coil

plane is considered. This cylinder that serves as the target is shifted in a range between 0 mm

and 12 mm, with a step of 1 mm. For each of these shifted cases, a rotation range from 0 to

90 degrees with steps of 1 degree is constructed, with the average field distribution in the

target cylinder with this specific combination of spatial shift and rotation angle evaluated.

The average field distributions are then plotted on the two-dimensional grid, as shown in Fig.

4.5.
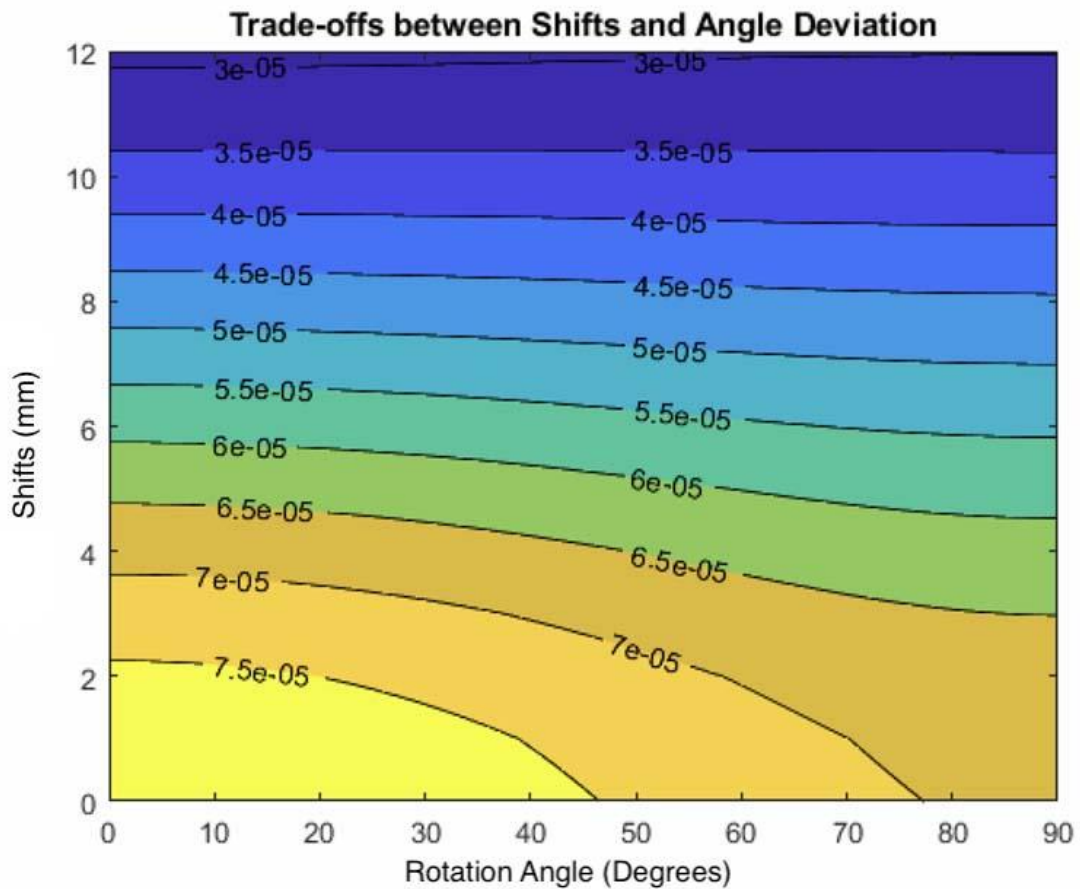
Figure 4.5 Trade-offs between shifts (mm) and rotation angle (deg). When shifted to the boundary of the coil, the effective magnetic flux density (T) is decreased by ~46%. When combining the effects of rotation and deviation together, the rotation angle will have a greater effect on the coil performance. If the target is placed near the boundary of the loop, the effects of rotation angle will be considerably smaller.

However, a more common situation is to place the target object near the region below the center of the coil. This indicates that to achieve the desired high-SNR image, the coil should still be placed as flat as possible when placed near the region below coil center.

One of the most essential aspects to be studied is the heating effect. In the human head model for SAR simulation, the maximum local SAR presented in the brain region is 0.039597 W/kg. The average SAR and temperature fluctuation in the pituitary region are 0.7337 W/kg and

0.0674 K respectively. This can be explained by the fact that the pituitary is placed right in the back of the coil, and is thus much closer to the excitation source, having a stronger field distribution.
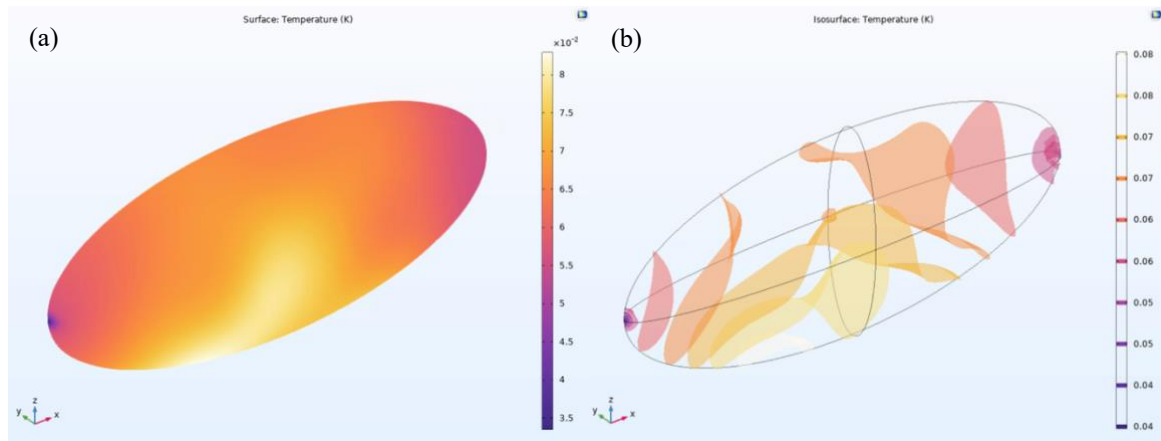
Figure 4.6 Temperature variations of the pituitary region. **(a)** Surface temperature increase. **(b)** Iso-surface plot showing the increment of temperature within the pituitary region.

From the plots, we can see that the highest SAR occurs near the surface, adjacent to the feed point of the figure-8 coil in the air cavity. Referring to the local SAR limitation of 2 W/kg for the brain, the SAR values presented in this study is well below the threshold. On the other hand, the maximum temperature incrementation ~0.08 K is also much smaller than the limitation of 3.5 °C that would cause severe physical damage to the brain. However, the temperature variation distribution in the human brain model induced by the figure-8 coil placed inside the air cavity is not directly related to the SAR distribution. This might be caused by the effect of dielectric properties, thermal properties, blood perfusion, and penetration depth of the electromagnetic power [45].
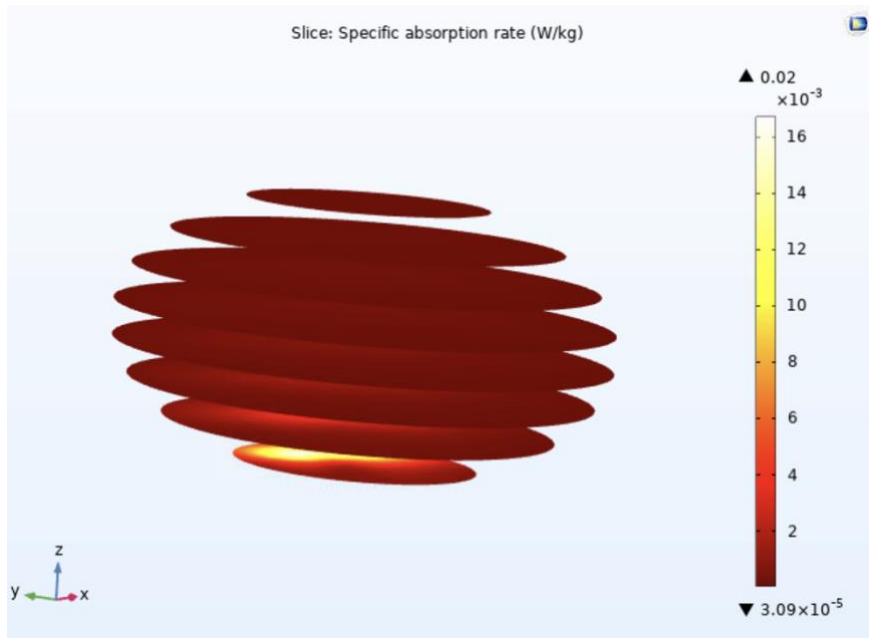
Figure 4.7 SAR distribution. The region that is close to the coil presents the largest SAR.

5. Discussions and Conclusions

In this work, we discuss the optimal coil design for the application of pituitary tumor detection. The optimal selections of radius and interval (i.e., distance between the two legs) are discussed. The effect of rotation is also studied and compared with the performance of a single-loop coil. Finally, the effect of shifting the relative position of the pituitary below the coil plane is studied and the compensation between shifting and rotating is discussed. In this section, we will review important details of this specific coil design, analyze the limitations, and propose potential steps for future studies.

5.1. Discussions

A circular-shaped figure-8 coil is selected to fit into the cavity above the pituitary to image in proximity. The optimal radius of figure-8 coils is studied and applied to the pituitary imaging case. A radius of 10 mm is selected to produce the maximum field distribution for the given target depth (compared to the performance of coils with different radius). The minimum span of the cavity if measured horizontally (parallel to the main magnetic field) is approximately 20 mm based on clinical data, which means that the selected coil of 10 mm radius would fit into the majority of the patient's cavity.

The size of the cavity varies for different patients. In the extreme cases where the patients have smaller span of the cavity (compared to the selected figure-8 coil size) in the direction parallel to the main field, directly placing the coil horizontally is impossible. In this situation, rotating the coil plane provides a way to place the coil properly. If rotating the coil plane from 0 to ~30 degrees, the increment of usable cavity space for coil placement is normally within

5mm. If the coil plane is rotated for more than 30 degrees, a more significant increase for the upper limit of the allowable coil size is possible. Hence, rotation can provide extra freedom for the actual placement of the coil in operations, especially in the case that the cavity is too small to hold the coil of selected size horizontally (i.e., parallel to the main magnetic field).

In general, coils with larger radius can image deeper into the target region. The rotation of coils can either facilitate the placement of regular-sized coil into a small cavity or enable the possibility of fitting bigger coils to take a deeper look into the region of interests. However, the rotation of coil often comes with the cost of degrading image quality, which is essentially the case for the previous design of single loop coils. These single loop coils are limited by the "dead spot" in the center when rotated 90 degrees and are subject to a more significant degradation in signal intensity during rotation. The circular shaped figure-8 coil design contributes to solving the problem of the "dead spot" and severe signal drops during rotation by providing a more stabilized rotation-related performance. However, the figure-8 coil design comes with a decrease in the average signal intensity (~70%) compared to the original signal loop design based on simulation results.

The structure of the coil is also studied, including the optimal distance between the two components in series (or interval/leg distance). Coil designs with smaller intervals generate stronger fields on the center axis, and the optimal interval is determined to be $\leq$ 2 mm. 2 mm is selected as a representative of the optimal intervals. Optimization of other details of the coils (i.e., subtle structures of the two-layer design, the connecting components between the two components in series, and the leg details) shall be discussed in future studies.

Sometimes it is not possible to place the center of the coil directly above the pituitary. When the coil is placed horizontally (0 deg rotation), the pituitary to be imaged can be near the boundary of the coil in extreme cases. Rotating the coil plane can help with shifting the relative position of the pituitary closer to the center. The signal intensity increases by more than 2 times if the relative position of the pituitary is shifted from the boundary of the coil plane to the center. Also, rotation will not have an observable effect for figure-8 coil if the target object is near the boundary of the coil. This indicates that for the pituitary-near-the-boundary cases, rotating the coil plane and thus shifting the coil towards the center will contribute to an increase in the signal intensity, since the trivial effects of rotation itself cannot endanger the overall performance.

The SAR distribution and temperature variations induced by the figure-8 coil placed inside the cavity are also studied. The local SAR and temperature change are far below the threshold that would lead to a severe damage to the brain, demonstrating the safety of this application.

5.2. Limitations and Future Steps

The currently discussed radius and intervals are optimized and selected for a target object placed right below the coil plane. Potential validations include a full scan of all the possible placements of the targeted pituitary below the coil plane for the radius and interval optimization. Also, the mesh size in the simulation will affect the accuracy and smoothness of the resulted curve. For example, when rectangular shaped mesh grids are applied in model building process with circular shaped target regions selected for mathematical analysis, the approximation of the data points in the boundary can be problematic. Hence, a finer model

with smaller mesh size can potentially improve the accuracy of the model, with the cost of greatly increasing computation time (i.e., for each individual iteration and the tuning-and-matching time for each model).

On the other hand, this work is simulation-based optimization. To validate the optimal coil parameters selected, phantom experiments will be performed after the completion of this thesis. Like the phantom validation mentioned in [4], an igloo cavity will be 3D-printed to mimic the sphenoid sinus (the cavity). Except for the printed figure-8 coil attached to the "floor", this cavity will only contain air. A resolution plate with holes of different diameters will be placed right beneath the igloo cavity, representing the ROIs. The imaging quality of the holes at different sizes can be used to evaluation the performance (or resolution) of the coil. The igloo cavity (with coil placed inside) and the resolution plate will be fixed inside a plastic jar, and the jar itself (including the holes of various sizes drilled on the resolution plate) will be filled with agar gel. The rotation angle of the coil plane can be simulated by adjusting the supporter that holds the jar. The coil inside the igloo cavity will be tuned and matched by a portable vector network analyzer (VNA).

The experimentally obtained scan signal SNR maps will be compared with the COMSOL generated plots of normalized amplitude of the effective magnetic field at different rotation angles. For different angles, the average value of the SNR obtained from scanning in the ROI will also be plotted and compared with the normalized average value of the effective magnetic fields in the target region obtained from simulations. This step validates the stability of the figure 8-shaped coil system in the presence of rotations. The performance of the

circular shaped figure-8 coils will be compared with that of the single loop coils.

Although the proposed figure 8-shaped coils show a better stability in rotation, it comes with the cost of slightly decreasing the overall effective field strength, and thus decreasing the maximum SNR achievable. One potential solution is to apply quadrature operation, where the design of the figure-8 coil is chosen to overlap with the single loop coil in the way that the mutual inductance between the two coils is minimized [46]. Theoretically, the fields generated by these two coils are orthogonal to each other and there should be a 90-degree phase shift between the two channels. For decoupled coils, the noise correlation between the two coils can be ignored, and the maximum achievable SNR by the quadrature operation is given by the square root of the sum of the squares of the maximum SNR achieved by both coils [46]. This leads to a $\sqrt{2}$ increase in the maximum achievable SNR in the case that two individual coils share SNRs of the same magnitude.

In summary, simulation-based coil designs should be continuously optimized to achieve higher SNR while taking safety restrictions into considerations. Experimental measurements should also be performed to validate the proposed model. We hope in the future, the pituitary gland imaging can be convenient, safe, and with high resolution.

Bibliography

[1] M. Varrassi *et al.*, "High-resolution magnetic resonance imaging at 3T of pituitary gland: advantages and pitfalls," *Gland Surg*, vol. 8, no. Suppl 3, pp. S208–S215, Sep. 2019, doi: 10.21037/gs.2019.06.08.

[2] A. Colao, M. Boscaro, D. Ferone, and F. F. Casanueva, "Managing Cushing's disease: the state of the art," *Endocrine*, vol. 47, no. 1, pp. 9–20, 2014, doi: 10.1007/s12020-013-0129-2.

[3] J. Zhai, W. Zheng, Q. Zhang, J. Wu, and X. Zhang, "Pharmacokinetic analysis for the differentiation of pituitary microadenoma subtypes through dynamic contrast-enhanced magnetic resonance imaging," *Oncol Lett*, vol. 17, no. 5, pp. 4237–4244, May 2019, doi: 10.3892/ol.2019.10083.

[4] J. Lin *et al.*, "A Miniature Flexible Coil for High-SNR MRI of the Pituitary Gland," *IEEE Access*, vol. 10, pp. 12619–12628, 2022, doi: 10.1109/ACCESS.2022.3143544.

[5] B. Gruber, M. Froeling, T. Leiner, and D. W. J. Klomp, "RF coils: A practical guide for nonphysicists," *Journal of Magnetic Resonance Imaging*, vol. 48, no. 3. John Wiley and Sons Inc., pp. 590–604, Sep. 01, 2018. doi: 10.1002/jmri.26187.

[6] M. Alfonsetti *et al.*, "Versatile coil design and positioning of transverse-field RF surface coils for clinical 1.5-T MRI applications," *MAGMA*, vol. 18, pp. 69–75, Jun. 2005, doi: 10.1007/s10334-004-0090-4.

[7] Z.-P. Liang Lauterbur Paul C. IEEE Engineering in Medicine and Biology Society., "Principles of magnetic resonance imaging: a signal processing perspective," 2000.

[8] F. A. M. Cappabianco, C. S. Shida, and J. S. Ide, "Introduction to Research in Magnetic

Resonance Imaging," in *2016 29th SIBGRAPI Conference on Graphics, Patterns and Images Tutorials (SIBGRAPI-T)*, 2016, pp. 1–14. doi: 10.1109/SIBGRAPI-T.2016.010.

[9]   C. R. Jack, R. C. Petersen, P. C. O'Brien, and E. G. Tangalos, "MR-based hippocampal volumetry in the diagnosis of Alzheimer's disease," *Neurology*, vol. 42, no. 1, p. 183, Jan. 1992, doi: 10.1212/WNL.42.1.183.

[10]   M. Filippi *et al.*, "MRI criteria for the diagnosis of multiple sclerosis: MAGNIMS consensus guidelines," *Lancet Neurol*, vol. 15, no. 3, pp. 292–303, Mar. 2016, doi: 10.1016/S1474-4422(15)00393-2.

[11]   L. Tanenbaum, "3T MRI in clinical practice," *Appl Radiol.*, vol. 34, pp. 8–17, Jan. 2005, doi: 10.37549/AR1312.

[12]   J. Jerrolds and S. Keene, "MRI Safety at 3T versus 1.5T," 2008.

[13]   D. I. Hoult, "The NMR receiver: A description and analysis of design," *Progress in Nuclear Magnetic Resonance Spectroscopy*, vol. 12, no. 1, pp. 41–77, 1978, doi: https://doi.org/10.1016/0079-6565(78)80002-8.

[14]   J. J. H. Ackerman, T. H. Grove, G. G. Wong, D. G. Gadian, and G. K. Radda, "Mapping of metabolites in whole animals by 31P NMR using surface coils," *Nature*, vol. 283, no. 5743, pp. 167–170, 1980, doi: 10.1038/283167a0.

[15]   S. Melmed, "Pituitary tumors," *Endocrinol Metab Clin North Am*, vol. 44, no. 1, pp. 1–9, Mar. 2015, doi: 10.1016/j.ecl.2014.11.004.

[16]   V. Singh, "Study on Design Development of Magnetic Resonance Imaging (MRI) System," vol. Volume 4, pp. 2456–8457, Sep. 2019.

[17]   P. Keller and M. Instruments, "Technologies for precision magnetic field mapping,"

Geneva: Metrolab Instruments, 2007.

[18] Z. Liu, F. Jia, J. Hennig, and J. Korvink, "Optimization MRI Cylindrical Coils Using Discretized Stream Function with High Order Smoothness," *IEEE Transactions on Magnetics - IEEE TRANS MAGN*, vol. 48, pp. 1179–1188, Mar. 2012, doi: 10.1109/TMAG.2011.2171355.

[19] S. S. Hidalgo-Tobón, "Theory of gradient coil design methods for magnetic resonance imaging," *Concepts in Magnetic Resonance Part A*, vol. 36, pp. 223–242, 2010.

[20] P. C. LAUTERBUR, "Image Formation by Induced Local Interactions: Examples Employing Nuclear Magnetic Resonance," *Nature*, vol. 242, no. 5394, pp. 190–191, 1973, doi: 10.1038/242190a0.

[21] C. E. G. Salmon, E. L. G. Vidoto, M. J. Martins, and A. Tannús, "Optimization of saddle coils for magnetic resonance imaging," *Brazilian Journal of Physics*, vol. 36, no. 1a, Mar. 2006, doi: 10.1590/S0103-97332006000100004.

[22] "RF Coils ... They've Come a Long, Long Way," *GE Healthcare*, vol. 1, 2005.

[23] C. E. Hayes and L. Axel, "Noise performance of surface coils for magnetic resonance imaging at 1.5 T.," *Med Phys*, vol. 12 5, pp. 604–7, 1985.

[24] A. Kumar and P. A. Bottomley, "Optimized quadrature surface coil designs," *MAGMA*, vol. 21, no. 1–2, pp. 41–52, Mar. 2008, doi: 10.1007/s10334-007-0090-2.

[25] S. TOLANSKY, "Negative Nuclear Spins and a Proposed Negative Proton," *Nature*, vol. 134, no. 3375, p. 26, 1934, doi: 10.1038/134026a0.

[26] D. Leitão, R. P. A. G. Teixeira, A. Price, A. Uus, J. v Hajnal, and S. J. Malik, "Efficiency analysis for quantitative MRI of T1 and T2 relaxometry methods," *Phys Med Biol*, vol.

66, no. 15, p. 15NT02, Jul. 2021, doi: 10.1088/1361-6560/ac101f.

[27] J. Mispelter and M. Lupu, "Homogeneous resonators for magnetic resonance: A review," *Comptes Rendus Chimie*, vol. 11, no. 4, pp. 340–355, 2008, doi: https://doi.org/10.1016/j.crci.2007.10.003.

[28] D. Hoult and R. Deslauriers, "A high-sensitivity, high-B1 homogeneity probe for quantitation of metabolites," *Magnetic resonance in medicine: official journal of the Society of Magnetic Resonance in Medicine / Society of Magnetic Resonance in Medicine*, vol. 16, pp. 411–417, Dec. 2005, doi: 10.1002/mrm.1910160307.

[29] D. I. Hoult and B. Tomanek, "Use of Mutually inductive coupling in probe design," *Concepts in Magnetic Resonance*, vol. 15, pp. 262–285, Dec. 2002, doi: 10.1002/cmr.10047.

[30] S. S. Eaton Eaton Gareth R. Berliner Lawrence J., *Biomedical EPR. Pt. B. Methodology, instrumentation, and dynamics*. New York: Kluwer Academic Publishers, 2005.

[31] S. Oh, A. G. Webb, T. Neuberger, B. Park, and C. M. Collins, "Experimental and numerical assessment of MRI-induced temperature change and SAR distributions in phantoms and in vivo," *Magn Reson Med*, vol. 63, no. 1, pp. 218–223, Jan. 2010, doi: 10.1002/mrm.22174.

[32] Y. Seo and Z. J. Wang, "Measurement and evaluation of specific absorption rate and temperature elevation caused by an artificial hip joint during MRI scanning," *Scientific Reports*, vol. 11, no. 1, p. 1134, 2021, doi: 10.1038/s41598-020-80828-7.

[33] Y. Seo and Z. J. Wang, "MRI scanner-independent specific absorption rate measurements using diffusion coefficients," *Journal of Applied Clinical Medical*

Physics, vol. 18, pp. 224–229, 2017.

[34] J. Allison and N. Yanasak, "What MRI Sequences Produce the Highest Specific Absorption Rate (SAR), and Is There Something We Should Be Doing to Reduce the SAR During Standard Examinations?," *American Journal of Roentgenology*, vol. 205, no. 2, pp. W140–W140, Jul. 2015, doi: 10.2214/AJR.14.14173.

[35] Prost JE, Wehrli FW, Drayer B, Froelich J, Hearshen D, and Plewes D, "SAR reduced pulse sequences," *Magn Reson Imaging*, vol. 6, no. 2, pp. 125–130, Mar. 1988, doi: 10.1016/0730-725x(88)90441-9.

[36] J. Yeung and A. Haouimi, "Signal-to-noise ratio (MRI)," *Reference article, Radiopaedia.org. (Accessed on 15 May 2022)*.

[37] A. Kumar, W. A. Edelstein, and P. A. Bottomley, "Noise figure limits for circular loop MR coils," *Magn Reson Med*, vol. 61, no. 5, pp. 1201–1209, May 2009, doi: 10.1002/mrm.21948.

[38] C.-Nien. Chen Hoult D. I., *Biomedical magnetic resonance technology*. Bristol: Institute of Physics Pub., 1995.

[39] W. Chunli, B. Zhiming, X. Jingkui, and W. Jinxing, "Simulation analysis on quality factor of RF receiving coil for an MRI system," in *2009 Chinese Control and Decision Conference*, 2009, pp. 4652–4655. doi: 10.1109/CCDC.2009.5191835.

[40] D. M. Hoang, E. B. Voura, C. Zhang, L. Fakri-Bouchet, and Y. Z. Wadghiri, "Evaluation of coils for imaging histological slides: signal-to-noise ratio and filling factor," *Magn Reson Med*, vol. 71, no. 5, pp. 1932–1943, May 2014, doi: 10.1002/mrm.24841.

[41] J. C. Lindon, George E. Tranter, and David Koppenaal, *Encyclopedia of spectroscopy*

and spectrometry. Academic Press, 2016.

[42] B. B. Beard *et al.*, "Comparisons of computed mobile phone induced SAR in the SAM phantom to that in anatomically correct models of the human head," *IEEE Transactions on Electromagnetic Compatibility*, vol. 48, no. 2, pp. 397–407, 2006, doi: 10.1109/TEMC.2006.873870.

[43] M. Levoy, "MRI data originally from Univ. of North Carolina (downloaded from the Stanford volume data archive at http://graphics.stanford.edu/data/voldata/)."

[44] J. W. Hand, R. W. Lau, J. J. W. Lagendijk, J. Ling, M. Burl, and I. R. Young, "Electromagnetic and Thermal Modeling of SAR and Temperature Fields in Tissue Due to an RF Decoupling Coil," 1999.

[45] T. Wessapan, S. Srisawatdhisukul, and P. Rattanadecho, "Specific absorption rate and temperature distributions in human head subjected to mobile phone radiation at different frequencies," *International Journal of Heat and Mass Transfer*, vol. 55, no. 1–3, pp. 347–359, Jan. 2012, doi: 10.1016/j.ijheatmasstransfer.2011.09.027.

[46] Giovannetti G *et al.*, "Design of a quadrature surface coil for hyperpolarized 13C MRS cardiac metabolism studies in pigs.," *Concepts in Magnetic Resonance Part B: Magnetic Resonance Engineering.*, vol. 43, no. 2, pp. 69–77, Apr. 2013.